
Article:
Zhou, H., Wagg, D. orcid.org/0000-0002-7266-2105 and Li, M. (2017) Equivalent force control combined with adaptive polynomial-based forward prediction for real-time hybrid simulation. Progress in Structural Engineering and Materials, 24 (11). e2018. ISSN 1365-0556

https://doi.org/10.1002/stc.2018

Structural Control and Health Monitoring

Equivalent Force Control Combined with Adaptive Polynomial-based Forward Prediction for Real-time Hybrid Simulation

Journal:	*Structural Control and Health Monitoring*
Manuscript ID	STC-16-0051.R2
Wiley - Manuscript type:	Research Article
Date Submitted by the Author:	n/a
Complete List of Authors:	Zhou, Huimeng; Key Laboratory of Earthquake Engineering and Engineering Vibration, Institute of Engineering Mechanics, China Earthquake Administration Wagg, David; University of Sheffield, Department of Mechanical Engineering Li, Mengning; Key laboratory of Earthquake Engineering and Engineering Vibration, Institute of Engineering Mechanics, China Earthquake Administration
Keywords:	Equivalent force control, Adaptive polynomial-based forward prediction, Time delay, Stability, Accuracy

Equivalent Force Control Combined with Adaptive Polynomial-based Forward Prediction for Real-time Hybrid Simulation

Huimeng Zhou[1*], David J. Wagg[2], Mengning Li[1]

1 Key Laboratory of Earthquake Engineering and Engineering Vibration, Institute of Engineering Mechanics, China Earthquake Administration

2 Department of Mechanical Engineering, University of Sheffield, Sheffield S1 3JD, U.K.

SUMMARY

The equivalent force control method uses feedback control to replace numerical iteration and solve the nonlinear equation in a real-time hybrid simulation via the implicit integration method. During the real-time hybrid simulation, a time delay typically reduces the accuracy of the test results and can even make the system unstable. The outer-loop controller of the equivalent force control method can eliminate the effect of a small time delay. However, when the actuator has a large delay, the accuracy of the test results is reduced. The adaptive forward prediction method offers a solution to this problem. Thus, in this paper, the adaptive polynomial-based forward prediction algorithm is combined with equivalent force control to improve the test accuracy and stability. The new method is shown to give good stability properties for a specimen with nonlinear stiffness by analyzing the location of the poles of the discrete transfer system. Simulations with linear and nonlinear specimens are then presented to demonstrate the effectiveness of this method. Finally, experimental results with a linear stiffness specimen and a magneto-rheological (MR) damper are used to demonstrate that this method has better accuracy than the equivalent force control method with non-adaptive delay compensation.

KEY WORDS: Equivalent force control; Adaptive polynomial-based forward prediction; Time delay; Stability; Accuracy

1. INTRODUCTION

Real-time hybrid simulation (RTHS) divides a structure into two parts: the critical element is taken as an experimental substructure, and the remainder of the structure is a numerical model in a computer. RTHS can be used to test full-scale specimens and estimate the dynamic performance of a structure relatively accurately [1-6].

The numerical integration algorithm is important for RTHS. The integration algorithm is typically either an explicit integration algorithm [1,4-6] or an implicit algorithm [3]. Traditional explicit integration algorithms [1] have conditional stability criteria. However, some explicit integration algorithms with unconditional stability have been proposed recently [4-6]. For example, the LRST algorithm [5] has unconditional stability for linear structures, which can be extended to nonlinear structures using a calculation of the Jacobi matrix of the structure for each time step. The CR [6] and KR-α [4] methods have unconditional stability for linear elastic and stiffness softening-type nonlinear systems. The implicit

algorithm [3] is generally unconditionally stable but requires numerical iteration.

Wu *et al*. [7, 8] proposed the equivalent force control (EFC) method, which solves the nonlinear equation of implicit integration via a so-called *equivalent force* feedback control to replace numerical iteration for RTHS. It uses the proportional plus derivative (PD) control as an outer controller. The PD control has a problem of steady-state error for nonlinear systems and the control system is easy to de-stabilize because of noise in the equivalent force (EF) feedback. These problems can be solved by using a proportional plus integral (PI) controller [9] or sliding mode control [10]. There is an equivalent force response delay in RTHS, which has an effect equivalent to negative damping [11]. The traditional solution [7, 8] is to increase the gain of the outer controller to cancel the time delay in the equivalent force response. However, a system with high controller gain is easier to destabilize because of the noise in the force and displacement responses. Thus, Shi *et al*. [12] used a Kalman filter to reduce the noise in the equivalent force response; as a result, the control gain can be set sufficiently high to cancel the time delay using this method.

The time delay for large tonnage dynamic actuators is always typically in the region of 20-80 ms [9, 10]. To track the equivalent force command, the control gain typically needs to be set to a very large value such that the magnitude plot $M(\omega)$ of the open loop transfer function of the EFC system near the natural frequency of the structure is a peak, thus resulting in greater susceptibility to instability [13]. To address this limitation, this paper presents a method in which the time delay compensation is applied outside the equivalent force control loop. As a result, the compensation is not affected by the noise in the equivalent force response. To achieve this a polynomial-based forward prediction [14] is used to extrapolate the EF command, which can be considered an expansion of the polynomial-based forward extrapolation [11, 15]. Because the delay time of the equivalent force response varies slightly depending on the excitation frequency, amplitude and specimen nonlinearity [15], the adaptive algorithm proposed by Wallace *et al*. [14] is used to tune the forward extrapolation parameters online. This method also has the advantage of being suitable for nonlinear specimens, which is an important characteristic for hybrid testing.

In fact, the development of adaptive algorithms to identify the time delay in RTHS tests has been considered by multiple other authors [16-21]. The adaptive polynomial-based forward prediction (AFP) algorithm was first proposed by Wallace *et al*. [14] to improve the stability and accuracy of RTHS for lightly damped systems [22]. Tu *et al*. [23] improved the AFP algorithm with respect to the settling performance and numerical conditions. To guarantee the stability, appropriate limiting values for the adaptive parameters k_a and P are proposed in this paper.

Other time delay compensation approaches typically use an inverse model compensation to cancel the dynamics of the transfer system, which are essentially implemented as a feedforward controller. They model the actuator-specimen as a first-order [3, 24] or third-order [2] model, respectively. The virtual coupling proposed by Christenson *et al*. [13] is a first-order inverse feedforward controller in essence, which was achieved by using a virtual structure concept.

As a result of the nonlinearity in a specimen, the dynamic characteristics of the actuator may change significantly. Thus, Philips *et al*. [25] proposed a new model-based servohydraulic tracking control method including feedforward-feedback links to achieve accurate tracking of a desired displacement in real time, which is a development of model-based compensation [2]. Moreover, Chen *et al*. [26] applied an adaptive control scheme to a model-based feedforward-feedback controller to accommodate specimen nonlinearity. The robust integrated actuator control proposed by Ou *et al*. [27] can also be considered a feedforward-feedback link, in which the loop shaping feedback control based on H∞ optimization is used as the feedback controller.

Liu *et al*. [28] used online delay estimation [15] to improve the performance of the model-based inverse

compensation. Chen *et al*. [29] proposed a dual compensation scheme, which designs an outer loop proportional controller to tune the inverse compensation procedure using the actuator tracking error. Chen *et al*. [30, 31] also proposed an adaptive inverse compensation method, which uses a PI controller to tune the inverse compensator using the tracking indicator (TI). The inverse compensation algorithms [3, 24-31] can also be used to improve the performance of the EFC. The procedure and principle of the EFC combined with the inverse compensation methods are similar to EFC combined with an AFP, which is not discussed further due to limited space. The purpose of the paper is to demonstrate that using EFC combined with AFP leads to a significant improvement in performance over EFC alone. Furthermore this combination also has very good performance when the experimental specimen is strongly nonlinear.

This paper is arranged as follows: first, an introduction of the EFC is given. Second, the formulation of the EFC combined with an AFP is described. Then, the stability and accuracy of this new method is analyzed. Finally, numerical simulations and actual tests are described to demonstrate the performance of this method.

2. OVERVIEW OF EFC

To study the equivalent force control method combined with an adaptive forward prediction (EFC-AFP), the formulation of the EFC [7] is introduced first. The equation of motion for a real-time hybrid simulation at step i+1 can be expressed in a time-discretized form as

$$\mathbf{M}_{\mathrm{N}}\mathbf{a}_{i+1}+\mathbf{C}_{\mathrm{N}}\mathbf{v}_{i+1}+\mathbf{R}_{\mathrm{N}}\left(\mathbf{d}_{i+1}\right)+\mathbf{R}_{\mathrm{E}}(\mathbf{a}_{i+1},\mathbf{v}_{i+1},\mathbf{d}_{i+1})=\mathbf{F}_{i+1} \tag{1}$$

where **M** and **C** are the mass and damping matrices, respectively, **R** is the restoring force vector, **d**, **v** and **a** are the displacement, velocity and acceleration vectors of the structure, respectively, and **F** is the excitation force vector. The subscript N denotes variables associated with the numerical substructure, and the subscript E denotes variables associated with the experimental substructure. It is assumed that the damping force is linearly proportional to the velocity and that $\mathbf{R}_{\mathrm{E}}$ is a function of the displacement, velocity and acceleration in general.

With the Newmark constant-average-acceleration method, the time-discretized equations of the acceleration and velocity approximations are expressed as

$$\mathbf{a}_{i+1}=\frac{4}{\Delta t^{2}}(-\mathbf{d}_{i}-\Delta t\mathbf{v}_{i}-\frac{\Delta t^{2}}{4}\mathbf{a}_{i}+\mathbf{d}_{i+1}) \tag{2}$$

$$\mathbf{v}_{i+1}=-\frac{2}{\Delta t}\mathbf{d}_{i}-\mathbf{v}_{i}+\frac{2}{\Delta t}\mathbf{d}_{i+1} \tag{3}$$

where Δt is the integration time interval. Substituting Equations (2) and (3) into (1) gives

$$\mathbf{R}_{\mathrm{N}}(\mathbf{d}_{i+1})+\mathbf{K}_{\mathrm{PD}}\mathbf{d}_{i+1}+\mathbf{R}_{\mathrm{E}}(\mathbf{a}_{i+1},\mathbf{v}_{i+1},\mathbf{d}_{i+1})=\mathbf{F}_{\mathrm{EQ},i+1} \tag{4}$$

where

$$\mathbf{K}_{\mathrm{PD}}=\frac{4\mathbf{M}_{\mathrm{N}}}{\Delta t^{2}}+\frac{2\mathbf{C}_{\mathrm{N}}}{\Delta t} \tag{5}$$

$$\mathbf{F}_{\mathrm{EQ},i+1}=\mathbf{F}_{i+1}+\mathbf{M}_{\mathrm{N}}\mathbf{a}_{i}+(\frac{4\mathbf{M}_{\mathrm{N}}}{\Delta t}+\mathbf{C}_{\mathrm{N}})\mathbf{v}_{i}+(\frac{4\mathbf{M}_{\mathrm{N}}}{\Delta t^{2}}+\frac{2\mathbf{C}_{\mathrm{N}}}{\Delta t})\mathbf{d}_{i} \tag{6}$$

where $\mathbf{K}_{\mathrm{PD}}$ is called the pseudodynamic stiffness [7]. $\mathbf{F}_{\mathrm{EQ},i+1}$ can be considered an equivalent force command that consists of the external force and the pseudodynamic effect and depends only on the previous step response. Equation (4) can be viewed as a hybrid dynamic equilibrium condition [7].

Equation (4) can also be interpreted as representing a hybrid force control system [7], in which the force

command is $\mathbf{F}_{EQ}$ and the hybrid plant to be driven consists of the physical part $\mathbf{R}_E$ and the numerical parts $\mathbf{K}_{PD}$ and $\mathbf{R}_N$. Fig. 1 gives the control block diagram for a real-time hybrid simulation with an EFC. There are two controllers in Fig. 1. The inner one is the traditional displacement controller of the actuator-specimen system. The outer one is an EFC controller that is used to enforce the equilibrium condition presented in (4). Because the inner loop is controlled in displacement mode, the equivalent force error after regulation of the outer loop controller is transformed into a displacement command $\mathbf{d}^c_{i+1}(t)$ by a conversion matrix $\mathbf{C}_F$. In this paper, $\mathbf{C}_F=(\mathbf{K}_E+\mathbf{K}_N+\mathbf{K}_{PD})^{-1}$, in which $\mathbf{K}_E$ and $\mathbf{K}_N$ are the initial stiffness of the experimental and numerical substructure, respectively. If the equivalent force response tracks the equivalent force command, the equilibrium condition given in (4) is satisfied, and the displacement command $\mathbf{d}^c_{i+1}$ is the correct solution for (4).

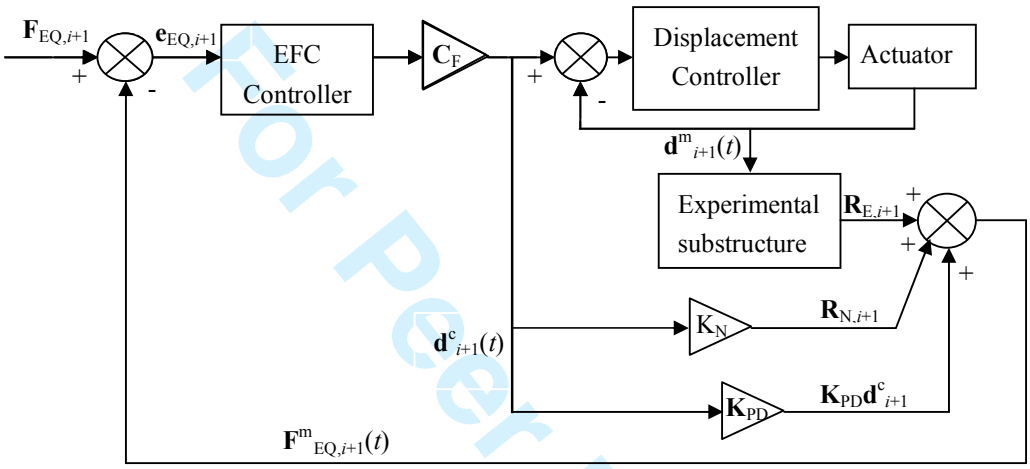

Figure 1. Block diagram of the EFC [7].

This process is the same as the modified iterative procedure [32]. An EFC controller calculates $\mathbf{u}$ in every sampling time step. The substep number is determined as $k=\Delta t/t_s$, in which t_s is the sampling time step. The sampling time step is 0.001 s for this system; the iteration numbers are the same as the substep number. For example, when the time step Δt is 0.01 s, the sampling time step t_s is 0.001 s, and the iteration numbers are $k=\Delta t/t_s=10$. EFC tries to get the approximate exact solution of the nonlinear function consistently with minimal error by designing the controller in an equivalent force control loop [8-10]. The convergence criterion for the EFC method is the equivalent force error between the equivalent force command and response. If the equivalent force error is equal to 0, convergence is assured. In actuality, the equivalent force error can only be close to 0 because of control error. Thus, a correction to displacement $\mathbf{d}_{i+1}$ is used, as shown in Equation (7). However, the convergence criteria cannot be satisfied in a time step when there is large time delay. Thus, the AFP algorithm is used outside the equivalent force control loop to compensate for the time delay and guarantee that the convergence criterion is satisfied. To ensure the equilibrium of Equation (4), the displacement $\mathbf{d}_{i+1}$ is updated [7] at the end of the time step, as described below.

$$\mathbf{d}_{i+1}=\frac{\mathbf{F}_{EQ,i+1}-\mathbf{R}_{E,i+1}}{\mathbf{K}_{PD}+\mathbf{K}_N} \tag{7}$$

3. FORMULATION OF EFC COMBINED WITH AFP ALGORITHM

The adaptive polynomial-based forward prediction algorithm was proposed by Wallace et al. [13] and is used herein to compensate for the time delay in the equivalent force system, as shown in Fig. 2. It is located outside the equivalent force control loop to compensate for the time delay of a RTHS test system. The adaptive algorithm uses the EF error between the EF command and response to tune the adaptive parameters P and k_a in the forward prediction algorithm, as shown in Fig. 3. In this figure, there are three controllers in the EFC combined with AFP algorithm. The innermost controller is the displacement controller for the actuator, which is primarily to guarantee the stable displacement control for the actuator-specimen system. The middle-loop controller is the equivalent force controller, which is mainly used to guarantee the stable force control for the equivalent force control system. The outmost controller is the AFP controller, which is finally to guarantee the equilibrium condition of the equivalent force system shown as Equation (4) in spite of strong nonlinearity.

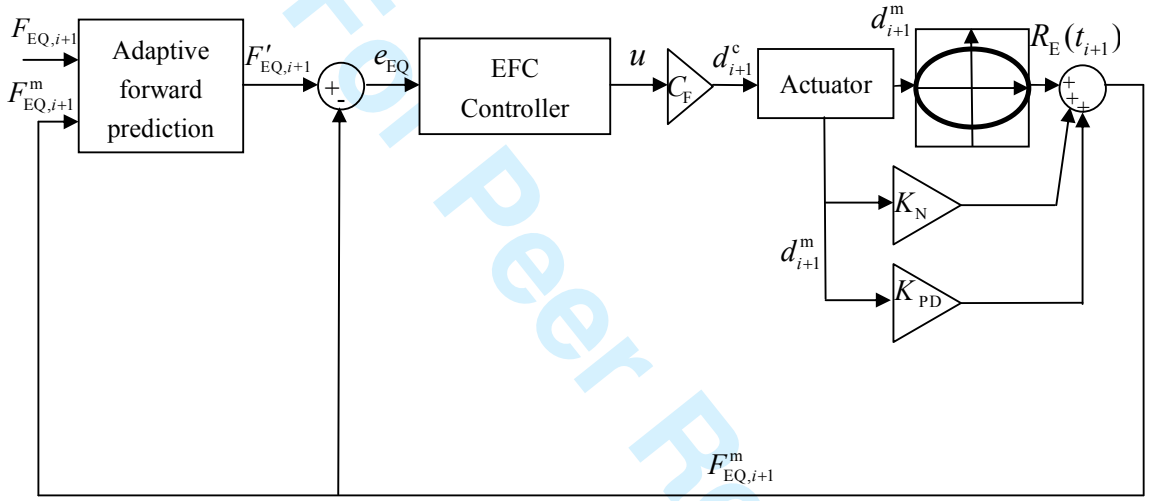

Figure 2. Block diagram of EFC combined with AFP algorithm.

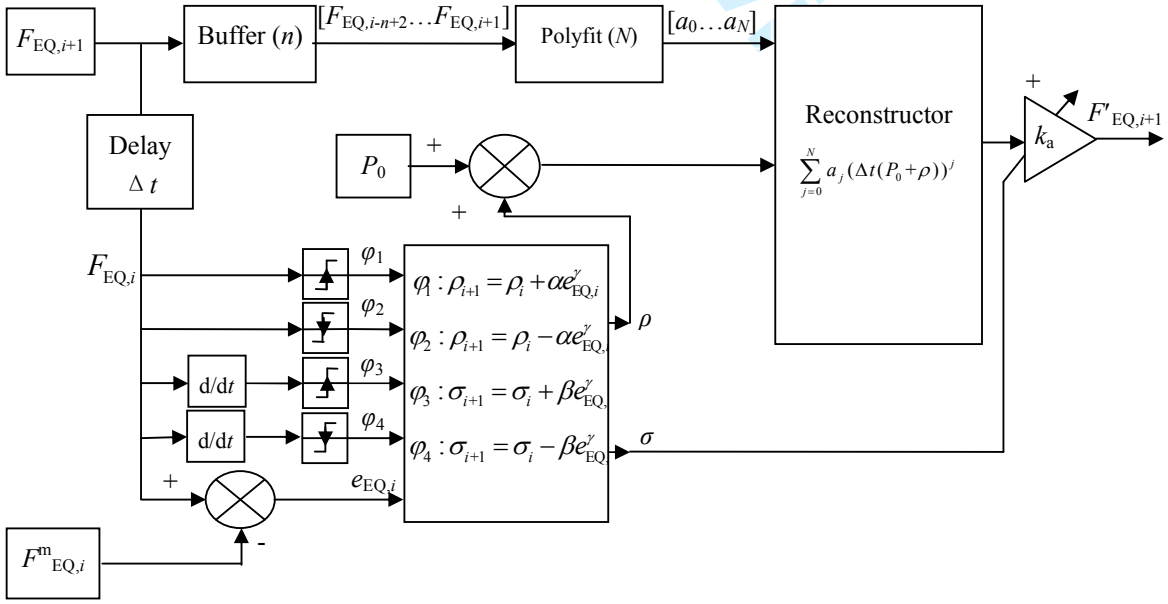

Figure 3. Block diagram of AFP algorithm [33].

For prediction of the equivalent force command signal, we assume that the equivalent force can be represented by a polynomial in t of order N with coefficients a_i (i=0, …, N), given by

$$F_{\mathrm{EQ}} = a_0 + a_1 t + \cdots + a_N t^N \tag{8}$$

when n data points are available, i.e.,

$$\begin{bmatrix} F_{\mathrm{EQ},i+1} \\ F_{\mathrm{EQ},i} \\ \vdots \\ F_{\mathrm{EQ},i-n+2} \end{bmatrix} = \begin{bmatrix} 1 & t_{i+1} & \cdots & t_{i+1}^N \\ 1 & t_i & \cdots & t_i^N \\ \vdots & \vdots & \vdots & \vdots \\ 1 & t_{i-n+2} & \cdots & t_{i-n+2}^N \end{bmatrix} \begin{bmatrix} a_0 \\ a_1 \\ \vdots \\ a_N \end{bmatrix} \tag{9}$$

Using a standard least-square method, the polynomial coefficient vector $\mathbf{a}$= $[a_0, \ldots, a_N]^{\mathrm{T}}$ can be obtained as

$$\mathbf{a} = \left(\mathbf{X}^{\mathrm{T}}\mathbf{X}\right)^{-1}\mathbf{X}^{\mathrm{T}}\mathbf{F}_{\mathrm{EQ}} \tag{10}$$

in which

$$\mathbf{X} = \begin{bmatrix} 1 & 0 & \cdots & 0 \\ 1 & -\Delta t & \cdots & (-\Delta t)^N \\ \vdots & \vdots & \vdots & \vdots \\ 1 & -(n-1)\Delta t & \cdots & (-(n-1)\Delta t)^N \end{bmatrix} \tag{11}$$

where we assume t_{i+1}=0 for simplicity and $\mathbf{F}_{\mathrm{EQ}}$=$[F_{\mathrm{EQ},i+1}, F_{\mathrm{EQ},i}, \ldots, F_{\mathrm{EQ},i-n+2}]^{\mathrm{T}}$.

The signal is predicted forward P multiplied by the time step such that the equivalent force command gives

$$F'_{\mathrm{EQ}} = F_{\mathrm{EQ},i+P+1} = \begin{bmatrix} 1 & P\Delta t & \cdots & (P\Delta t)^N \end{bmatrix}\mathbf{a} \tag{12}$$

or

$$F'_{\mathrm{EQ}} = \sum_{j=0}^{N}\left[a_j (P\Delta t)^j\right] \tag{13}$$

To account for the amplitude error, the predicted equivalent force command F'_{EQ} is modified to be

$$F'_{\mathrm{EQ}} = k_{\mathrm{a}}\sum_{j=0}^{N}\left[a_j (P\Delta t)^j\right] \tag{14}$$

where k_{a} is the amplitude compensation parameter (representing the ratio between the input EF command and output EF response amplitudes).

The parameters P & k_{a} in (14) are related to delay and amplitude error, respectively, which may vary with time. To reflect the varying nature of these parameters, P and k_{a} are represented as

$$P = P_0 + \rho \tag{15}$$

$$k_{\mathrm{a}} = k_{\mathrm{a0}} + \sigma \tag{16}$$

where P_0 & k_{a0} are the initial values and ρ & σ are the varying parts of P & k_{a}. In many cases, the delay and amplitude error do not change very quickly; thus, we do not need to update them too frequently.

Wallace *et al*. [14] proposed that ρ and σ can be updated only in four triggered states, with

$$\rho_{i+1} = \rho_i \pm \text{sign}(e_{\text{EQ},i})\alpha \left| e_{\text{EQ},i} \right|^{\gamma} \tag{17}$$

$$\sigma_{i+1} = \sigma_i \pm \text{sign}(e_{\text{EQ},i})\beta \left| e_{\text{EQ},i} \right|^{\gamma} \tag{18}$$

where α and β are the adaptive gains, γ is the convergence rate gain, the ± sign depends on the triggered states, and e_{EQ} is the EF synchronization error. The parameter γ controls the convergence rate; the larger it is, the faster the convergence of P and k_{a} is. The three gains in Equations (17) and (18) can be determined via preliminary analysis (Section 5.2) or from test-based experience.

There are four trigger states, which are initiated by the equivalent force command because it is not significantly affected by noise. At the initial stage, all of the states are zero; when one of the trigger states is satisfied, that trigger state changes to 1, and the corresponding adaptive law will proceed. If all of them are not satisfied, these triggers stay at zero and the adaptive parameters are kept constant. Equation (17) is triggered only when the sign of $F_{\text{EQ},i}$ changes. The ± sign is positive when $F_{\text{EQ},i}$ increases, and vice versa. Equation (18) is triggered when $F_{\text{EQ},i}$ reaches a local maximum or minimum, or equivalently, $\dot{F}_{\text{EQ},i}$ changes its sign. The ± sign is positive when $\dot{F}_{\text{EQ},i}$ increases, and vice versa. We use a custom code in a Matlab function of the Simulink model to build a zero crossing block. A local maximum/minimum is defined by the zero crossing point of the equivalent force velocity and the change direction, e.g., a local maximum is defined as the zero crossing point of the equivalent force velocity with the velocity changing from positive to negative.

The required steps to implement the EFC-AFP method with an appropriate choice for the AFP parameters P, k_{a}, α, β and γ are as follows:

1, Design the actuator controller and determine the displacement transfer function of the actuator-specimen (shown in Figure 5) via an identification experiment.;

2, Design the equivalent force controller and conduct a predetermined equivalent force load test;

3, Conduct a test with no time delay compensation with small amplitude input.

4, Measure the time delay and amplitude error at the peak of the waveform;

5, Set the initial values of P and k_{a} based on step 3;

6, Set the limits for P and k_{a} via discrete analysis and the transfer function (Section 4, Equations (19)-(42));

7, Determine the parameters α, β and γ via preliminary analysis (according to Equations (17)-(18) and Section 5.2) or from test-based experience;

8, Tune the parameters α, β and γ to get the best compensation effect (according to Equations (17)-(18) and Section 5.2).

4. STABILITY OF THE EFC COMBINED WITH AN AFP ALGORITHM

The time delay compensation methods can be viewed as a type of nonlinear control method; thus, its stability is a key issue. Herein, the stability of the EFC combined with an AFP algorithm is analyzed by considering the specimen nonlinearity. Other than some adaptive compensation algorithms [16-18, 21], which use an adaptive algorithm to identify the model parameters, the AFP algorithm is an error-driven adaptive feedback controller [34]. Additionally, because the adaption only occurs at the set trigger conditions, i.e., $\varphi_{1,\ldots,}$ φ_4, the AFP algorithm is subject to a persistence of excitation [33] condition. For

simplicity, the stability of the system for linear specimens is analyzed via a discrete transfer function approach [35-38], supposing that the parameters P and k_a are fixed. Then, the limiting values for the adaptive parameters P and k_a are set based on the results of a linear discrete transfer function approach analysis. Then, the stability of this new method for a specimen with nonlinear stiffness is discussed. Two types of nonlinear structural behavior are considered: stiffening and softening behavior. The force-displacement (F-Δ) relationship for idealized stiffening and softening structures is shown in Fig. 4. For civil engineering structures, stiffening can occur in bridge structures with cables [35], whereas softening is common in steel and concrete structures that undergo inelastic deformations.

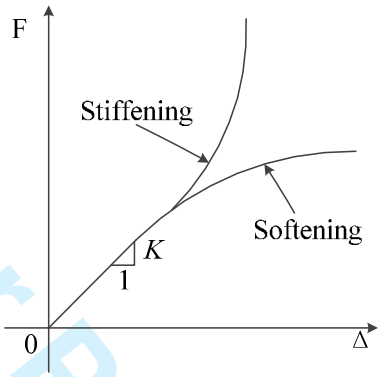

Figure 4. Definition of stiffening and softening behavior.

For the purpose of developing the transfer function for the EFC-AFP method, the tangent stiffness of an SDOF structure, represented by Equation (1), is assumed to be constant during the $(i+1)^{th}$ time step for a small value of Δt, whereby the restoring force for the $(i+1)^{th}$ time step can be expressed in terms of the displacement response d^m from the $(i)^{th}$ to $(i+1)^{th}$ time step, as follows:

$$R_{E,i+1} = R_{E,i} + K_t \cdot (d^m_{i+1} - d^m_i) \tag{19}$$

where K_t is the tangent stiffness of the experimental substructure for the $(i+1)$th time step. $R_{E,i+1}$ from Equation (19) is thus utilized in Equation (7) to represent $R_{E,i+1}$ and therefore to define the transfer function.

The block diagram representation of RTHS with an EFC-AFP algorithm is shown in Figure 5, in which j denotes the sub-step and k denotes the total number of sub-steps. The block servo-hydraulic actuator and servo controller represents the actuator-specimen system and actuator controller, whose input and output signals are the displacement (The detail is discussed in the end of Section 3).

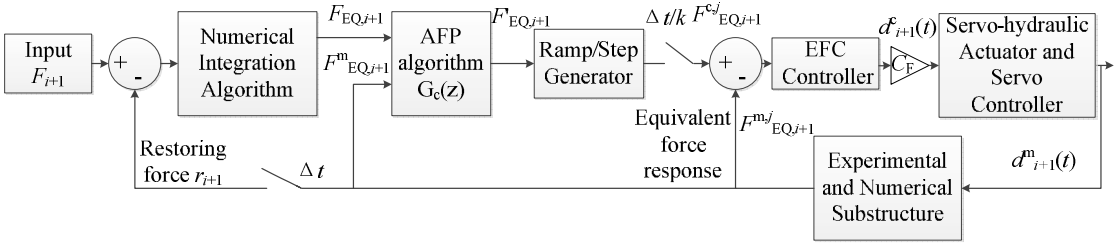

Figure 5. Block diagram of RTHS with an EFC-AFP algorithm, EFC controller and transfer function of actuator-specimen system.

For an SDOF structure, applying the discrete z-transform [39] to (6) and (7) yields

$$F_{\mathrm{EQ}}(z)=F(z)+M_{\mathrm{N}}\frac{a(z)}{z}+(\frac{4M_{\mathrm{N}}}{\Delta t}+C_{\mathrm{N}})\frac{v(z)}{z}+(\frac{4M_{\mathrm{N}}}{\Delta t^2}+\frac{2C_{\mathrm{N}}}{\Delta t})\frac{d(z)}{z} \tag{20}$$

$$d(z)=\frac{F_{\mathrm{EQ}}(z)-R_{\mathrm{E}}(z)}{K_{\mathrm{PD}}+K_{\mathrm{N}}} \tag{21}$$

where z is the complex variable in the discrete z-domain; $F(z)$, $a(z)$, $v(z)$, $d(z)$, $R_{\mathrm{E}}(z)$ and $F_{\mathrm{EQ}}(z)$ are the discrete z-transforms of the input excitation force, acceleration, velocity, displacement, restoring force and equivalent force command, respectively.

Applying the discrete z-transform to (2) and (3) yields

$$G_{vd}(z)=\frac{v(z)}{d(z)}=\frac{2(z-1)}{(z+1)\Delta t} \tag{22}$$

$$G_{ad}(z)=\frac{a(z)}{d(z)}=\frac{4(z-1)^2}{(z+1)^2\Delta t^2} \tag{23}$$

Substituting Equations (21), (22) and (23) into Equation (20) gives

$$F_{\mathrm{EQ}}(z)=\frac{1}{1-G'(z)}F(z)-\frac{G'(z)}{1-G'(z)}R_{\mathrm{E}}(z) \tag{24}$$

The numerator and denominator coefficients of discrete transfer function $G'(z)$ are tabulated in Table 1.

Table 1 Numerator and Denominator Coefficients of Discrete Transfer Function $G'(z)$

d_1	$4M_{\mathrm{N}}+2C_{\mathrm{N}}\Delta t+K_{\mathrm{N}}\Delta t^2$	n_1	0
d_2	$8M_{\mathrm{N}}+4C_{\mathrm{N}}\Delta t+2K_{\mathrm{N}}\Delta t^2$	n_2	$16M_{\mathrm{N}}+4C_{\mathrm{N}}\Delta t$
d_3	$4M_{\mathrm{N}}+2C_{\mathrm{N}}\Delta t+K_{\mathrm{N}}\Delta t^2$	n_3	$4C_{\mathrm{N}}\Delta t$

According to Equation (14), the formulation of $F'_{\mathrm{EQ},i+1}$ is a nonlinear function requiring the equivalent force command $F_{\mathrm{EQ},i+1}$, the order of polynomial N, the number of data n, the prediction step P, and the compensation parameter k_{a}. It becomes a nonlinear time-invariant function if the polynomial parameters N and n are determined. According to Equation (14), the discrete transfer function $G_{\mathrm{C}}(z)$ between the equivalent force command F_{EQ} and the prediction EF command F'_{EQ} and the formulations of $F'_{\mathrm{EQ},i+1}$ are tabulated in Table 2.

Table 2 Formulation of $F'_{\mathrm{EQ},i+1}$ and Discrete Transfer Function $G_{\mathrm{c}}(z)$

Polynomial parameters	Formulation of $F'_{\mathrm{EQ},i+1}$	Discrete transfer function $G_{\mathrm{c}}(z)$
N=1,n=2	$k_{\mathrm{a}}(1+P)F_{\mathrm{EQ},i+1}-k_{\mathrm{a}}PF_{\mathrm{EQ},i}$	$k_{\mathrm{a}}(1+P)-k_{\mathrm{a}}P\frac{1}{z}$
N=2,n=3	$k_{\mathrm{a}}(1+\frac{3}{2}P+\frac{P^2}{2})F_{\mathrm{EQ},i+1}-k_{\mathrm{a}}(P^2+2P)F_{\mathrm{EQ},i}$	$k_{\mathrm{a}}(1+\frac{3}{2}P+\frac{P^2}{2})-k_{\mathrm{a}}(P^2+2P)\frac{1}{z}$

	$+k_a(\frac{1}{2}P^2-\frac{P}{2})F_{EQ,i-1}$	$+k_a(\frac{1}{2}P^2-\frac{P}{2})\frac{1}{z^2}$
…	…	…

For example, when the polynomial parameters of the AFP algorithm are set as n=2 and N=1, the discrete transfer function $G_C(z)$ is

$$G_C(z)=\frac{F'_{EQ}(z)}{F_{EQ}(z)}=\frac{-k_aP+k_a(1+P)z}{z} \tag{25}$$

The selection of a suitable interpolation function to generate EF commands is important with respect to the resulting velocity and acceleration scheme. One simple choice is that the EF commands are constant during the time step such that

$$F^c_{EQ}(t)=F'_{EQ,i+1} \qquad i\Delta t\le t\le (i+1)\Delta t \tag{26}$$

Thus, the discrete transfer function between the modified EF command $F^c_{EQ}(z)$ and the prediction EF command $F'_{EQ}(z)$ is

$$G_{IP}(z)=\frac{F^c_{EQ}(z)}{F'_{EQ}(z)}=z \tag{27}$$

For the actuator control-loop system in continuous time, the 2nd-order differential equation is used to model the actuator

$$\ddot{d}^m+2\xi_A\omega_A\dot{d}^m+\omega_A^2d^m=\omega_A^2d^c \tag{28}$$

where d^m and d^c are the displacement response and command, respectively, and ω_A and ξ_A are the model parameters.

The PI controller is used as the EFC controller [9]. The sampling time step for the EFC controller is 0.001 s. From Fig. 1, the difference equations of the SDOF equivalent force control system can be obtained as

$$e^j_{EQ,i+1}=(F^{c,j}_{EQ,i+1}-F^{m,j}_{EQ,i+1}) \tag{29}$$

$$u^j_{i+1}=K_Pe^j_{EQ,i+1}+K_I\sum_1^{i\times n+j}\frac{1}{2}(e^j_{EQ,i+1}+e^{j-1}_{EQ,i+1})t_s \tag{30}$$

$$d^{c,j}_{i+1}=C_Fu^j_{i+1} \tag{31}$$

$$F^{m,j}_{EQ,i+1}=d^{m,j}_{i+1}(K_{PD}+K_N)+R^{m,j-1}_{E,i+1}+\Delta R^{m,j}_{E,i+1} \tag{32}$$

Assuming the tangent stiffness of the experimental substructure is constant during a step leads to

$$\Delta R^{m,j}_{E,i+1}=K_t(d^{m,j}_{i+1}-d^{m,j-1}_{i+1}) \tag{33}$$

where K_t is the tangent stiffness of the experimental substructure. For the sake of simplicity, the EFC controller can be equivalent to a continuous system because of the small sampling time step

$$u=K_Pe_{EQ}+K_I\int(F^c_{EQ}+F^m_{EQ}) \tag{34}$$

$$d^{\mathrm{c}} = C_{\mathrm{F}} u \tag{35}$$

$$F_{\mathrm{EQ},}^{\mathrm{m}} = d^{\mathrm{m}}(K_{\mathrm{PD}} + K_{\mathrm{N}}) + R_{\mathrm{E}}^{\mathrm{m}} \tag{36}$$

$$R_{\mathrm{E}}^{\mathrm{m}} = K_{\mathrm{t}} d^{\mathrm{m}} \tag{37}$$

Substituting Equations (28), (35), (36) and (37) into Equation (34) gives

$$\overline{b}_2 \dot{F}_{\mathrm{EQ}}^{\mathrm{c}} + \overline{b}_3 F_{\mathrm{EQ}}^{\mathrm{c}} = \dddot{d}^{\mathrm{m}} + \overline{a}_1 \ddot{d}^{\mathrm{m}} + \overline{a}_2 \dot{d}^{\mathrm{m}} + \overline{a}_3 d^{\mathrm{m}} \tag{38}$$

The coefficients of differential Equation (38) are expressed in terms of the structure and model parameters M_{N}, C_{N}, K_{PD}, K_{t}, C_{F}, ω_{A}, and ζ_{A} in Table 3.

Table 3 Coefficients of Differential Equation (38)

$\overline{a}_1$	$2\zeta_{\mathrm{A}}\omega_{\mathrm{A}}$	$\overline{b}_2$	$\mathrm{C}_{\mathrm{F}}\omega_{\mathrm{A}}^2 K_{\mathrm{P}}$
$\overline{a}_2$	$K_{\mathrm{P}}\mathrm{C}_{\mathrm{F}}\omega_{\mathrm{A}}^2(K_{\mathrm{PD}} + K_{\mathrm{N}} + K_{\mathrm{t}}) + \omega_{\mathrm{A}}^2$	$\overline{b}_3$	$K_{\mathrm{I}}\mathrm{C}_{\mathrm{F}}\omega_{\mathrm{A}}^2$
$\overline{a}_3$	$K_{\mathrm{I}}\mathrm{C}_{\mathrm{F}}\omega_{\mathrm{A}}^2(K_{\mathrm{PD}} + K_{\mathrm{N}} + K_{\mathrm{t}})$		

According to (26), the EF function is constant during the time step. The EFC system (38) is discretized by a zero-order-hold equivalent method [39] to get

$$G_{\mathrm{EQ}}(z) = \frac{\left(1-\frac{1}{z}\right) d^{\mathrm{m}}(z)}{\left(1-\frac{1}{z}\right) F_{\mathrm{EQ}}^{\mathrm{c}}(z)} = \frac{d^{\mathrm{m}}(z)}{F_{\mathrm{EQ}}^{\mathrm{c}}(z)} = \frac{\overline{n}_1 z^2 + \overline{n}_2 z + \overline{n}_3}{\overline{d}_0 z^3 + \overline{d}_1 z^2 + \overline{d}_2 z + \overline{d}_3} \tag{39}$$

where $d^{\mathrm{m}}(z)$ and $F^{\mathrm{c}}_{\mathrm{EQ}}(z)$ are the discrete z-transforms of the displacement response and modified EF command, respectively; $\overline{n}_3$, $\overline{n}_2$, $\overline{n}_1$ and $\overline{d}_3, \ldots, \overline{d}_0$ are the numerator and denominator coefficients of $G_{\mathrm{EQ}}(z)$, respectively, and 2 and 3 are the order of the polynomial for the numerator and denominator, respectively.

The discretized transfer function between the reaction force $R_{\mathrm{E}}(z)$ and the displacement response $d^{\mathrm{m}}(z)$ is

$$G_{\mathrm{R}}(z) = \frac{\left(1-\frac{1}{z}\right) R_{\mathrm{E}}(z)}{\left(1-\frac{1}{z}\right) d^{\mathrm{m}}(z)} = \frac{R_{\mathrm{E}}(z)}{d^{\mathrm{m}}(z)} = K_{\mathrm{t}} \tag{40}$$

The closed loop block diagram of the EFC-AFP system is shown in Fig. 6.

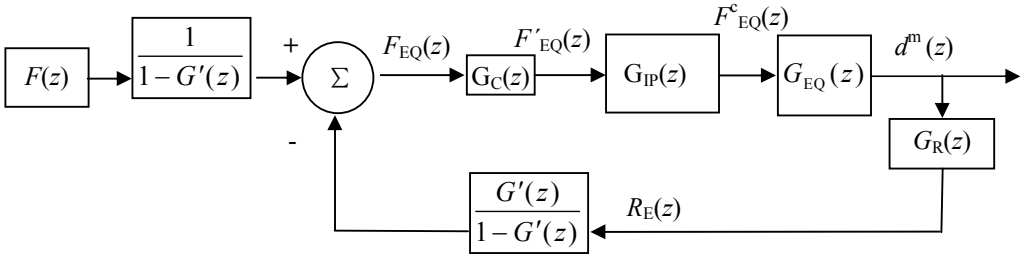

Figure 6. Closed loop block diagram for the EFC-AFP algorithm.

For nonlinear structures, the closed loop transfer function [36] between $F(z)$ and $d^{\mathrm{m}}(z)$ shown in Fig. 6 can be written in incremental form as

$$G(z)=\frac{\Delta d^{\mathrm{m}}(z)}{\Delta F(z)}=\frac{\frac{z-1}{z}d^{\mathrm{m}}(z)}{\frac{z-1}{z}F(z)}=\frac{G_{\mathrm{C}}(z)G_{\mathrm{IP}}(z)G_{\mathrm{EQ}}(z)}{1-G'(z)+G'(z)G_{\mathrm{C}}(z)G_{\mathrm{EQ}}(z)G_{\mathrm{R}}(z)} \tag{41}$$

where the increments $\Delta d^{\mathrm{m}}(z)$ and $\Delta F(z)$ are defined as $\Delta d^{\mathrm{m}}(z)=d^{\mathrm{m}}{}_{i+1}(z)-d^{\mathrm{m}}{}_{i}(z)$ and $\Delta F(z)=F_{i+1}(z)-F_i(z)$, respectively. The numerator and denominator coefficients for the discrete transfer function are expressed in terms of structure parameters M_{N}, C_{N}, K_{PD}, K_{t}, C_{F} and Δt.

When the specimen is linear, i.e., $K_{\mathrm{t}}=K_{\mathrm{E}}$, the closed loop transfer function can be obtained as

$$G(z)=\frac{d^{\mathrm{m}}(z)}{F(z)}=\frac{G_{\mathrm{C}}(z)G_{\mathrm{IP}}(z)G_{\mathrm{EQ}}(z)}{1-G'(z)+G'(z)G_{\mathrm{C}}(z)G_{\mathrm{EQ}}(z)G_{\mathrm{R}}(z)} \tag{42}$$

where the numerator and denominator coefficients for the discrete transfer function (42) are expressed in terms of structure parameters M_{N}, C_{N}, K_{PD}, K_{E}, C_{F} and Δt.

The closed loop transfer function between the EF command and response can be written in incremental form as

$$G_{cl}(z)=\frac{\Delta F^{\mathrm{m}}_{\mathrm{EQ}}(z)}{\Delta F_{\mathrm{EQ}}(z)}=\frac{\frac{z-1}{z}F^{\mathrm{m}}_{\mathrm{EQ}}(z)}{\frac{z-1}{z}F_{\mathrm{EQ}}(z)}=\frac{(1-G'(z))G_{\mathrm{C}}(z)G_{\mathrm{IP}}(z)G_{\mathrm{EQ}}(z)}{1-G'(z)+G_{\mathrm{C}}(z)G_{\mathrm{IP}}(z)G_{\mathrm{EQ}}(z)G_{\mathrm{R}}(z)G'(z)} \tag{43}$$

where the increments $\Delta F_{\mathrm{EQ}}(z)$ and $\Delta F^{\mathrm{m}}{}_{\mathrm{EQ}}(z)$ are defined as $\Delta F_{\mathrm{EQ}}(z)=F_{\mathrm{EQ},i+1}(z)-F_{\mathrm{EQ},i}(z)$ and $\Delta F^{\mathrm{m}}{}_{\mathrm{EQ}}(z)=F^{\mathrm{m}}{}_{\mathrm{EQ},i+1}(z)-F^{\mathrm{m}}{}_{\mathrm{EQ},i}(z)$, respectively.

The transfer function between the EF command and response can be written in incremental form as

$$G_{\mathrm{fd}}(z)=\frac{\Delta F^{\mathrm{m}}_{\mathrm{EQ}}(z)}{\Delta F_{\mathrm{EQ}}(z)}=\frac{\frac{z-1}{z}F^{\mathrm{m}}_{\mathrm{EQ}}(z)}{\frac{z-1}{z}F_{\mathrm{EQ}}(z)}=G_{\mathrm{C}}(z)G_{\mathrm{IP}}(z)G_{\mathrm{EQ}}(z) \tag{44}$$

When the poles of the characteristic function of the closed loop transfer function $G(z)$ are all located inside the unit circle, the test system is stable [35]. Because the adaptive parameters P and k_{a} change during the test, improper algorithm parameter design may produce unstable poles. If the actuator model is known and the specimen is linear ($K_{\mathrm{E}}=K_{\mathrm{t}}$), a stable range for P and k_{a} can be calculated. Furthermore, the limiting values for the prediction parameter P and amplitude gain k_{a} can be set according to the analysis. Then, the

stability of this method for a nonlinear system is discussed.

For example, the parameters of an SDOF structure adopted for numerical simulations are: M_N= 6658.24×10^3 kg, K_N=131.43×10^6 Nm^{-1}, K_E=131.43×10^6 Nm^{-1}, ζ_N=0.05 and C_E=0, which result in a structural period of 1 s. The parameters of the EFC controller and the AFP algorithm are K_P=0.1, K_I=80, N=4, and n=5. The actuator transfer function model is $T_P(s)$=(11.41s^2-8113.28s+2.954×10^6) (s^3+451.73s^2+62126.9s+ 2.956×10^6)$^{-1}$.

The maximum modulus of the poles of the characteristic function, i.e., (42), is defined as p. The stability ranges for the parameters P and k_a are shown in Fig. 7(a) and 7(b). Fig. 7(a) shows that there is a stability limit for the parameter P because the max modulus of poles is larger than 1 when the parameter P is larger or less than the constant values. The stability limit of P is affected by the parameter k_a (e.g., the stability range for P is reduced when the parameter k_a=1.1908 rather than k_a=1). From Fig. 7(b), it is also clear that there is a stability limit for k_a, which is affected by the parameter P. Note that the upper stability limit for k_a is very large when P=1.26 (the optimal value for P is 0.76 and the optimal parameter for k_a is 0.9908) because the overcompensation effectively adds additional damping. To ensure the stability of the system, the limiting values for the parameters P and k_a are, respectively, set as [0.26$\leqslant P\leqslant$1.26] and [0.7908$\leqslant k_a\leqslant$1.1908].

When the SDOF structure develops nonlinear behavior, the stability of the EFC-AFP can be investigated by analyzing the poles of the discrete transfer function [36] by systematically varying the structural properties (K_E, K_t) and the parameters P and k_a. The stability limit is established for a selected set of values for K_E, K_t, P, k_a, and the time step Δt by assigning the magnitude of the poles to be 1.0. Fig. 7(c) shows the results of the stability analysis of the EFC-AFP algorithm for four selected cases using different parameter combinations of P and k_a, i.e., [P, k_a]=[0.26, 0.7908], [0.76, 0.9908], [0, 1] and [1.26, 1.1908]. In Fig. 7(c), the stability limit for each case is expressed in terms of values of $\Omega=\omega_n\bullet\Delta t$ as a function of α_t. The parameter α_t is the degree of nonlinearity in the structure and is the ratio K_t/K_E, while ω_n is the elastic natural frequency of the SDOF structure. Fig. 7(c) shows that EFC-AFP has a finite stability limit when $0<\alpha_t<1$ and $\alpha_t>1$, indicating that the system is conditionally stable. For each of the four cases in Fig. 7(c), the EFC-AFP is shown to have a larger stability limit for a softening structure (i.e., when $\alpha_t<1$) than that for a stiffening structure (i.e., when $\alpha_t>1$). It can also be observed that EFC-AFP (the selected cases using the parameters [P, k_a]=[0.26, 0.7908], [0.76, 0.9908] and [1.26, 1.1908]) has a larger stability limit than the EFC method (a selected case using the parameters [P, k_a]=[0, 1]).

The algorithm is unconditionally stable when the experimental structure is perfectly plastic (i.e., α_t=0), where the stability limit is at infinity (in Fig. 7(c), the value of $\omega_n\bullet\Delta t$ is shown plotted to a value of 628950). When the structure develops perfectly plastic behavior, the restoring force of the experiment is a constant value during the time step, and when used in Equation (19), an accurate value of the predicted displacement d_{i+1} is achieved. Thus the stability of the system is the same as that of the Newmark constant-average-acceleration method.

The relationship between the stiffness nonlinearity and system stability with ω_n=6.28 and Δt=0.01 s is shown in Fig. 7(d). As shown, the stability upper limit value of α_t is 8.9 for the EFC. However, the stability limit value of the EFC-AFP algorithm expands to 25.64. Thus, the EFC combined with an AFP algorithm has better stability properties for stiffness compared to the EFC algorithm in this case.

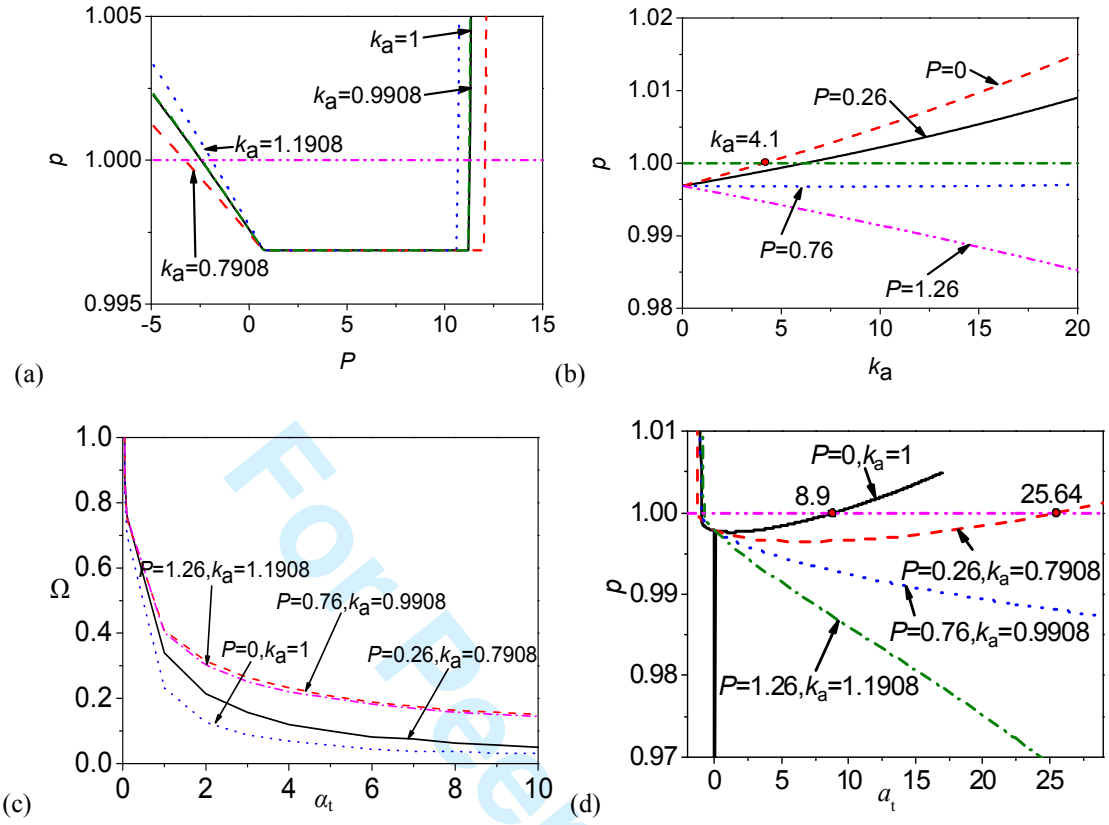

Figure 7. Stability of the EFC combined with an AFP. (a) Stability range for the parameter P; (b) Stability range for the parameter k_a; (c) Effect of α_t on the stability limit of the EFC-AFP; (d) Stability range for the parameter α_t.

Because the effect of the parameters P and k_a on the stability is coupled, to prove the stability of the system with the adaptive parameters P and k_a in the limiting range, the intensity plot of the stability of the EFC combined with an AFP is shown in Fig. 8 for the linear structure. The z coordinate value is the maximum modulus of the poles of the characteristic function (42). On the right side, a color bar shows the value of z; the regions bounded by the red dashed box represent the bounded domain. Fig. 8 shows that the system is always stable when the parameters k_a and P are in the bounded domain (because the value of the maximum modulus of the poles is smaller than 1). Thus, the stability of the system with k_a and P in the bounded domain is not affected by the adjustment of the parameters P and k_a; however, the adaptive parameters are varied either continuously or at four trigger conditions [14].

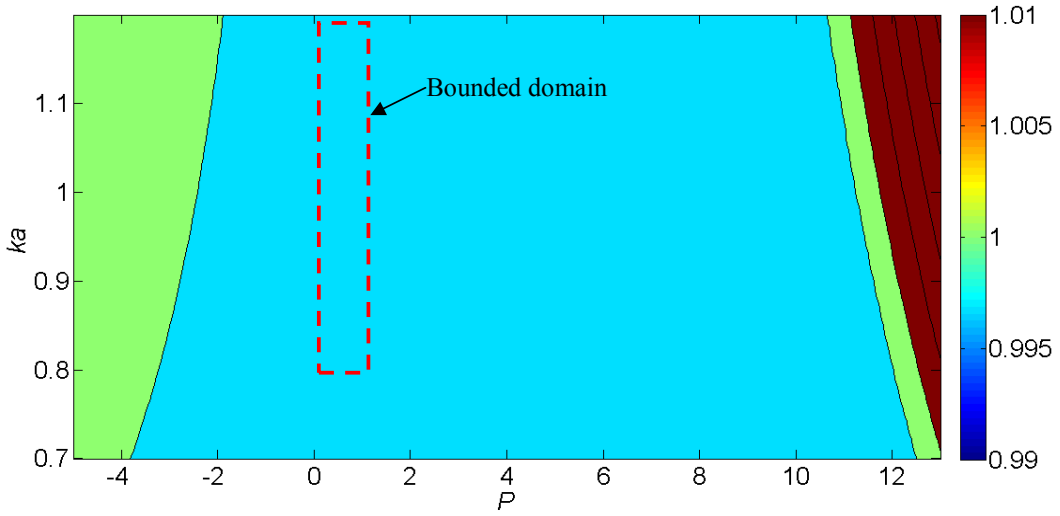

Figure 8. Intensity plot of the stability of the EFC combined with AFP

The accuracy of the EFC-AFP system can be presented by using a Bode diagram [38] according to Equation (44), which includes the EFC closed-loop system and AFP algorithm. Thus, the transfer function between the EF command and response of the EFC-AFP algorithm is analyzed in the frequency domain, as shown in Fig. 9.

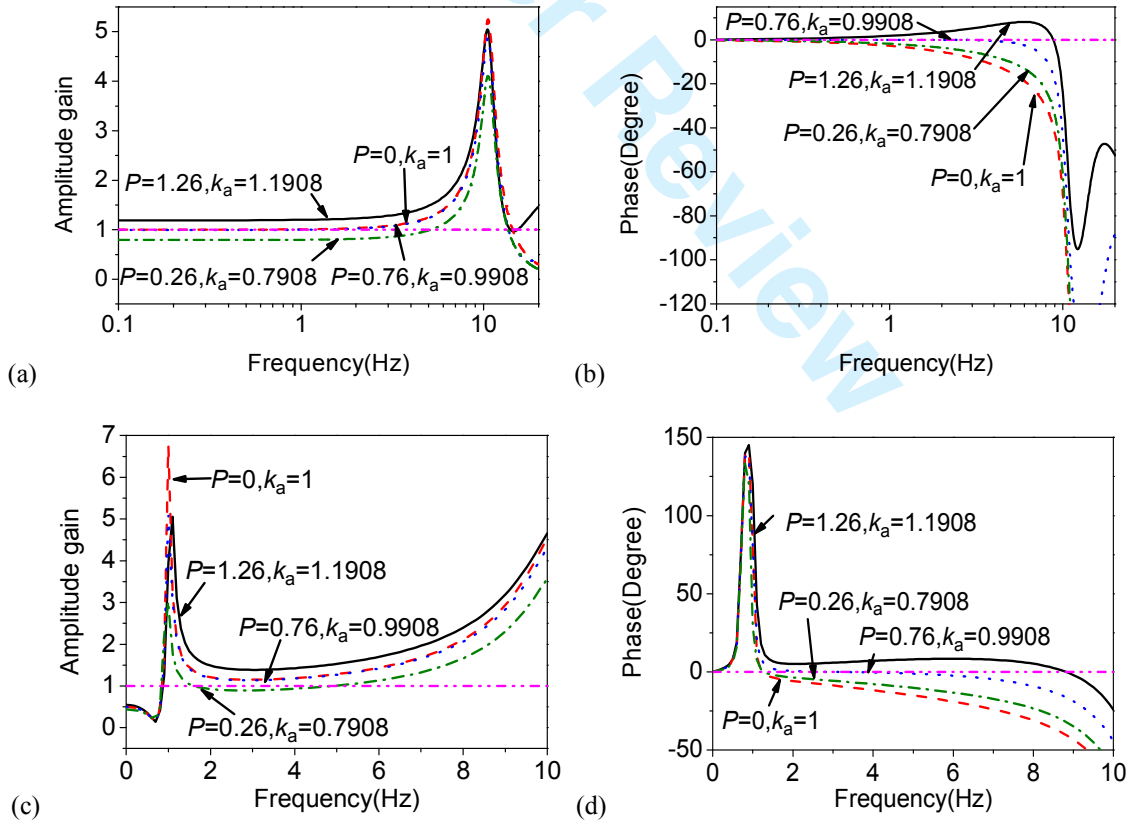

Figure 9. Bode diagram of the transfer function between the EF command and response of the EFC-AFP. (a)

Amplitude characteristic of Bode; (b) Phase characteristic of Bode; (c) Amplitude characteristic of closed-loop Bode; (d) Phase characteristic of closed-loop Bode.

Fig. 9 shows that the EFC-AFP algorithm can compensate for the dynamics of the system accurately in the 0-10 Hz frequency range. Moreover, the performance of the EFC-AFP algorithm with the limiting values for the parameters P and k_a is slightly superior to that of the AFP without compensation from the phase characteristic. There is a resonance peak approximately 10 Hz for the EFC system; the AFP algorithm cannot eliminate this characteristic because it depends on the inherent dynamics of the actuator. The closed loop transfer functions of the EFC-AFP system from Equation (43) are shown in Figure 9(c) and 9(d). From the figure, it can be observed that the AFP algorithm can add damping around the natural frequency and can improve the phase characteristics of the closed-loop system.

5. NUMERICAL SIMULATION

5.1 Numerical simulation of RTHS with the stiffness specimen

Numerical simulations are conducted in the time domain with Matlab™. The schematic diagram of the SDOF structure, with a spring as an experimental substructure, is shown in Fig. 10. The tangent stiffness of the spring, K_t, is related through $K_t=\alpha_t K_E$ to the initial stiffness, K_E, which is used to determine the displacement-force conversion factor C_F. The nonlinear specimen has a bilinear stiffness, with two linear stiffnesses represented by the coefficients: $\alpha_t=1$ and $\alpha_t=9$, defining the stiffness curve (see Fig. 11(d)).

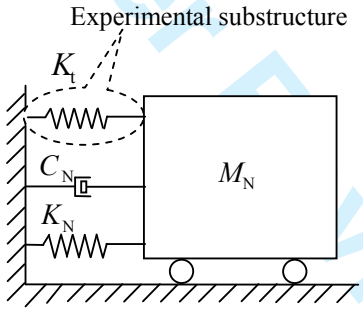

Figure 10. The substructured SDOF system.

The other parameters are: M_N= 6658.24×10^3 kg, K_N=131.43×10^6 Nm^{-1}, and K_E=131.43×10^6 Nm^{-1}, which result in a structural period of 1 s; ζ_N=0.05 and C_E=0. The third-order transfer function model of the actuator-specimen system is used [10]: $T_P(s)=(11.41s^2-8113.28s+2.954\times10^6)(s^3+451.73s^2+62126.9s+2.956\times10^6)^{-1}$. The integration time interval Δt is 0.01 s. The EFC controller parameters are K_P=0.1 and K_I=80. The adaptive forward prediction algorithm parameters are P_0=0.76 and k_{a0}=0.9908 (they are close to the optimal parameters P and k_a), N=4, n=5, $\alpha=10^{-15}$, $\beta=5\times10^{-17}$, and γ=2. The limiting values for the parameters P and k_a are, respectively, set as [0.26$\leqslant P\leqslant$1.26] and [0.7908$\leqslant k_a\leqslant$1.1908].

The displacement response and force-displacement relationship for the experimental substructure subject to the El Centro (NS, 1940) earthquake, with a peak acceleration of 0.0125g, is shown in Fig. 11. Fig. 11(a-c) show that the seismic responses obtained by the EFC combined with an AFP algorithm match the exact solution well. However, the responses of the EFC without delay compensation are unstable when the initial stiffness is underestimated, as shown in Fig. 11(c). Note that the parameter α_t is 9 in Fig. 11(d), which is larger than 8.9, which was the limiting value for stability derived in Section 4.

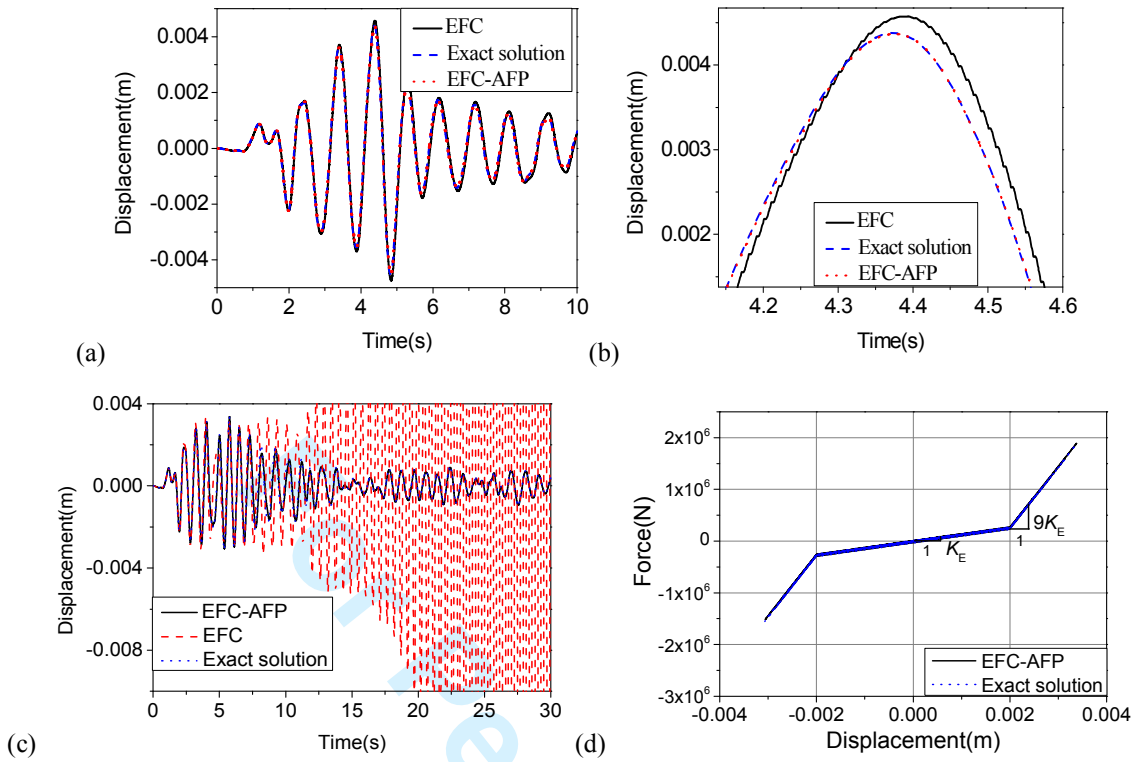

Figure 11. Numerical simulation of seismic responses. (a) Linear specimen: global view; (b) Linear specimen: enlarged view; (c)Nonlinear specimen: global view; (d) Nonlinear specimen: force-displacement relationship for experimental substructure.

5.2 Numerical simulation analysis of the adaptive variables

The selection of the data point number n and the order of polynomial N were discussed particularly by Wallace *et al*. [33] and Tu *et al*. [22]. To give guidance for the selection of the parameters α, β, and γ, the effect on performance is analyzed below. Note that the limiting values for P and k_a are not set in the following simulations to make the phenomenon more obvious. The parameters of the EFC controller are K_P=0.5 and K_I=36. The adaptive forward prediction parameters are P_0=1 (the optimal value of P_0 is 2.3), k_{a0}=1.0043, N=4, n=5, α=10^{-15}, and β=5×10^{-17}. The parameters of the structural model are the same as those of the linear SDOF structure in Section 5.1. The earthquake record (El Centro (NS, 1940)), with a peak acceleration of 0.0125g, is used as the input. The resulting displacement responses of the EFC combined with an AFP algorithm with different γ are shown in Fig. 12.

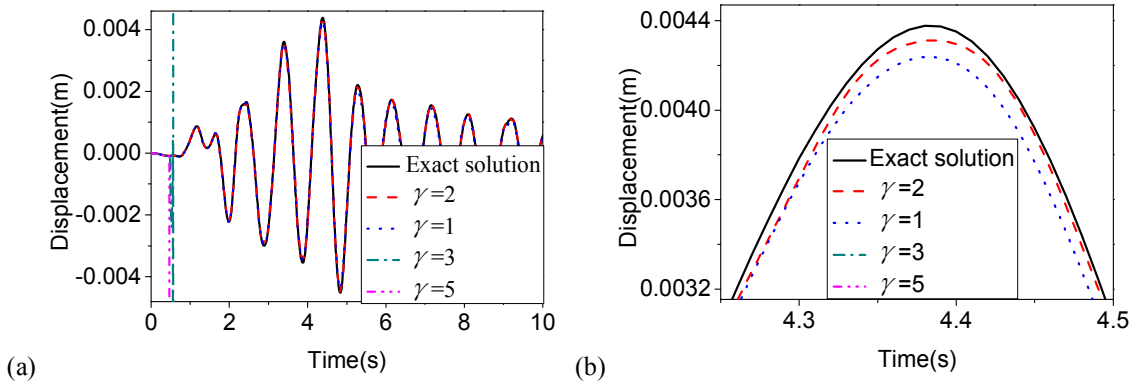

Figure 12. Displacement response for earthquake input. (a) Global map of displacement response comparison; (b) Enlarged view of displacement response comparison.

When γ is set as 3 and 5, the system is unstable because the parameters k_a and P are increased to $(1, 17.08)$ and $(1, 7.56\times10^{12})$, respectively, which are outside the stability range of the parameters P and k_a. Because the equivalent force error is larger than unity, the parameter γ cannot be set too large. Fig. 12(b) reveals that the greater the value of γ, the faster the tuning process. Fig. 12(b) shows that the displacement response with γ=2 is the closest to the exact value of displacement. The parameter γ is set as 2 in the subsequent simulation and experiment. The displacement of the EFC-AFP algorithm with different β is shown in Fig. 13.

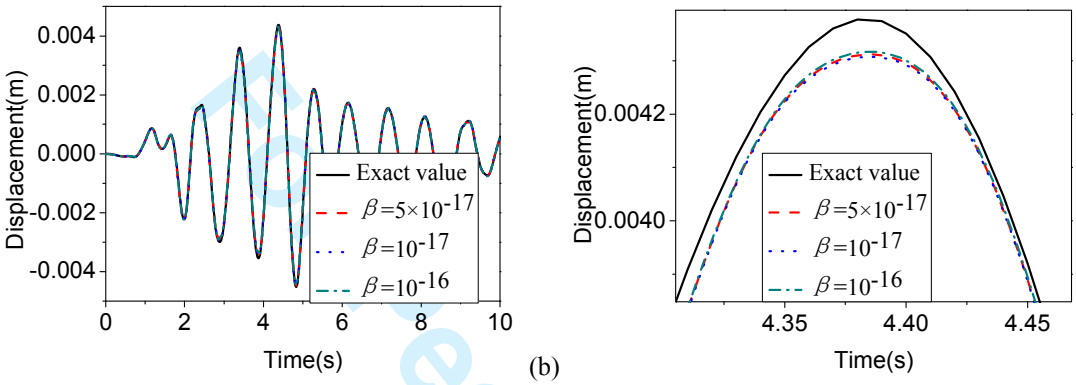

Figure 13. Displacement response for earthquake input. (a) Global map of displacement response comparison; (b) Enlarged view of displacement response comparison.

Fig. 13 shows that the compensation effect is better when the value of β is larger.

The displacement of the EFC-AFP algorithm with different α is shown in Fig. 14.

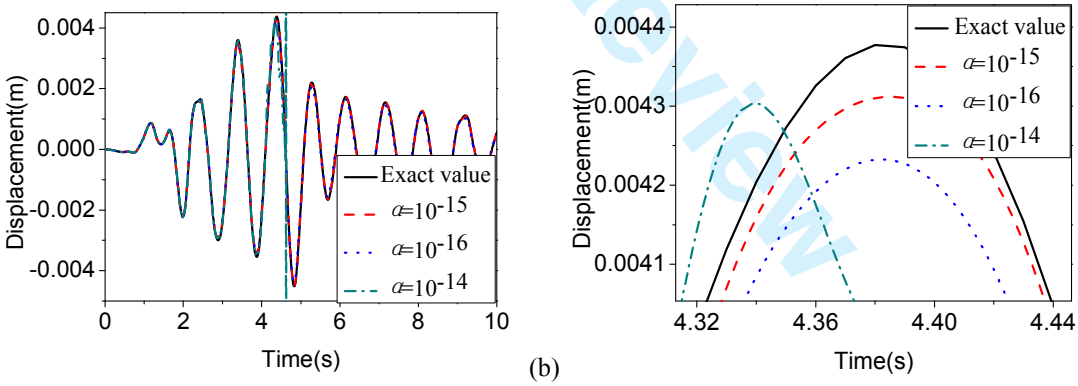

Figure 14. Displacement response for earthquake input. (a) Global map of displacement response comparison; (b) Enlarged view of displacement response comparison.

Fig. 14 shows that the compensation effect is improved when the value of α is set larger. However, the parameter α cannot be set too large, for example, the system will be unstable when the parameter $\alpha\geq10^{-14}$.

6. EXPERIMENTAL INVESTIGATION

For the hybrid simulation, we used a Simulink block to formulate a model and a dSPACE DS1104 R&D Controller Board to implement in real time. The sampling frequency of the dSPACE digital controller was

1000 Hz.

The schematic diagram of the SDOF structure, with a spring as an experimental substructure, is shown in Fig. 10. Fig. 15 shows the substructured model set-up, along with the transfer system that imposes the interface displacement on the physical substructure. A PI controller was used to control the actuator, with controller gains k_P=20 and k_I=0.15. For the EFC in this experimental study, an EFC controller with gains K_P=1.8 and K_I=16 was adopted. Through system identification in some pre-tests, the spring was found to have a stiffness of K_E=7912.6 Nm^{-1} and a damping coefficient of c=0.6 Nsm^{-1}. The parameters of the SDOF structure were: M_N=400.857 kg, K_N=7912.6 Nm^{-1}, and ζ_N=0.02, resulting in a natural period of 1 s. The integration interval Δt was 0.01 s. The hybrid simulation was carried out at the Bristol Laboratory for Advanced Dynamics Engineering, University of Bristol.

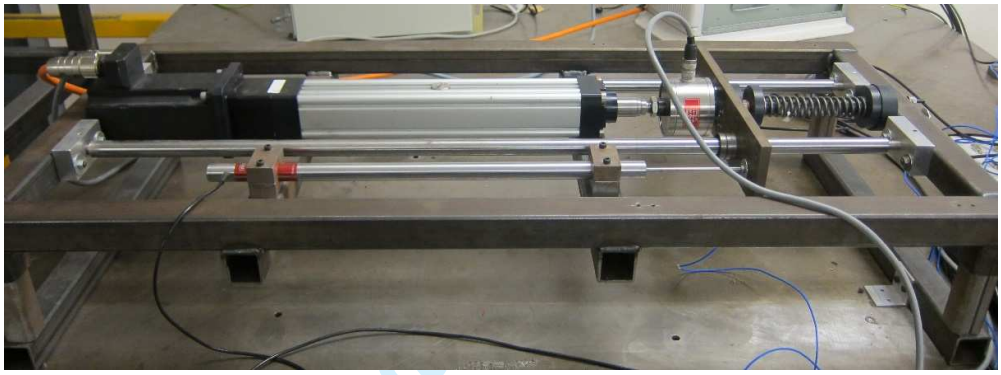

Figure 15. Experimental set-up of substructured model.

The step responses of displacement and equivalent force are shown in Fig. 16 and 17, respectively. It can be seen that the responses tracked the command well. The setting time for both displacement and equivalent force was approximately 0.25 s.

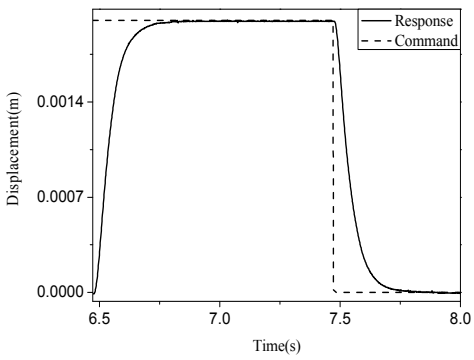

Figure 16. Step response of displacement

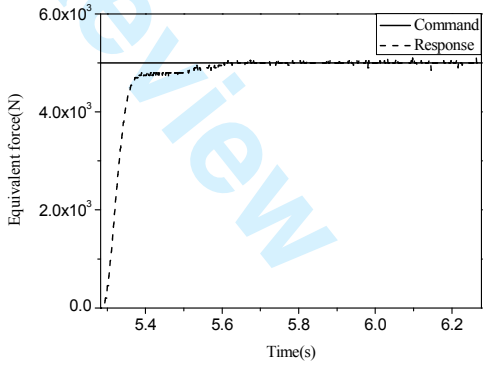

Figure 17. Step response of equivalent force response

6.1 Spring specimen real-time hybrid simulation

The earthquake input equivalent force and displacement responses of the RTHS from El Centro earthquake excitation of 0.009g peak acceleration are shown in Fig. 18. In this case, the EFC controller gains are K_P=1.6 and K_I=18; the displacement controller gains are k_P=20 and k_I=0.15; the AFP algorithm parameters are N=3, n=5, P_0=5.5, $k_{a,0}$=1.135, α=9×10^{-8}, β=4.5×10^{-9}, and γ=2; the limiting values for the parameter P are set as [-0.5 10.5]; the limiting values for the parameter k_a are set as [0.935 1.335]. The EF response is multiplied by 4.5 from the EFC for El Centro earthquake excitation with peak acceleration of 0.002g. The

EFC controller gains are K_P=1.6 and K_I=18, and the displacement controller gains are k_P=20 and k_I=0.15.

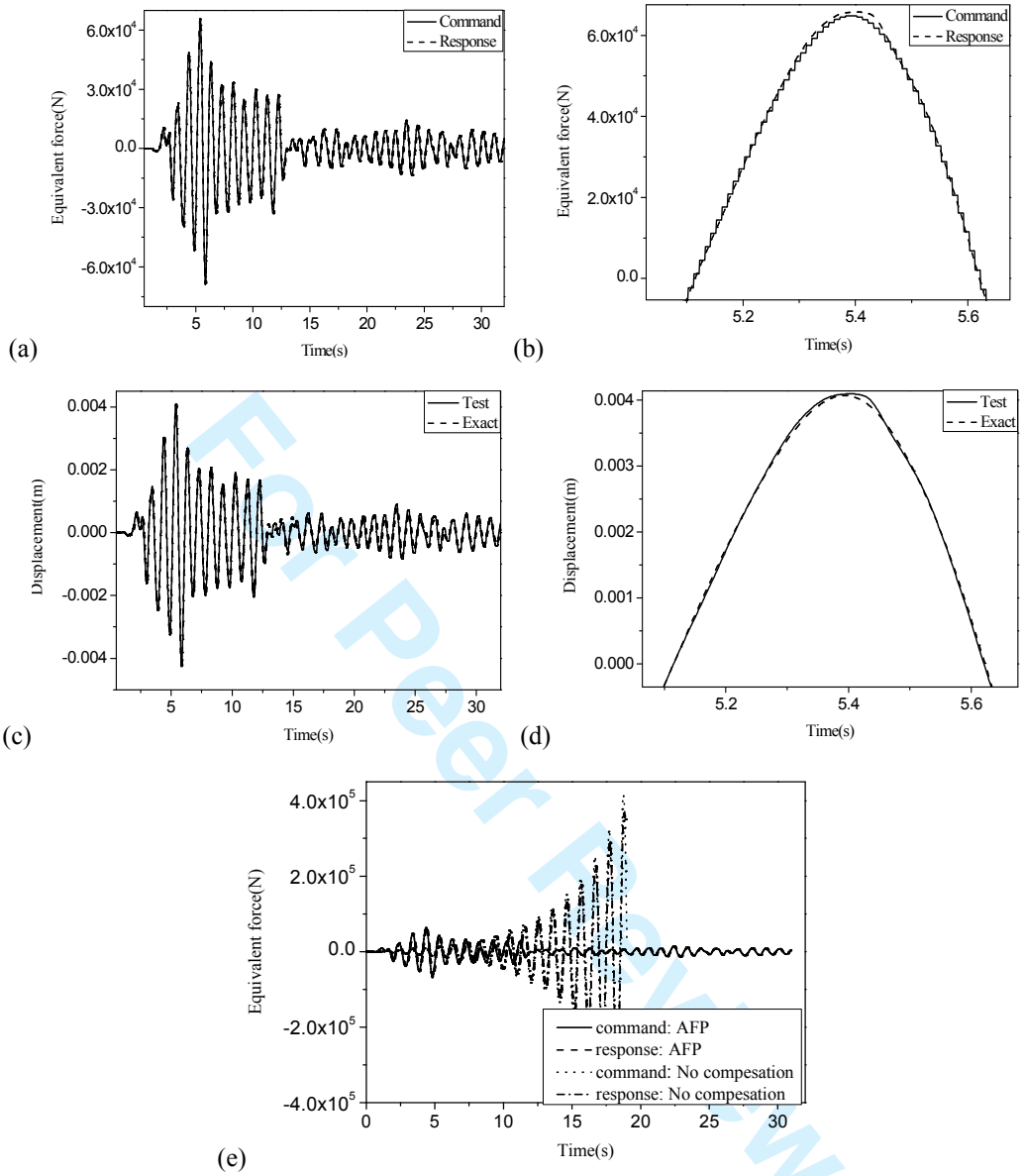

Figure 18. Equivalent force and displacement response. (a) Equivalent force response; (b) Enlarged view of equivalent force response; (c) Displacement response; (d) Enlarged view of displacement response; (e) EF response compared to EF command.

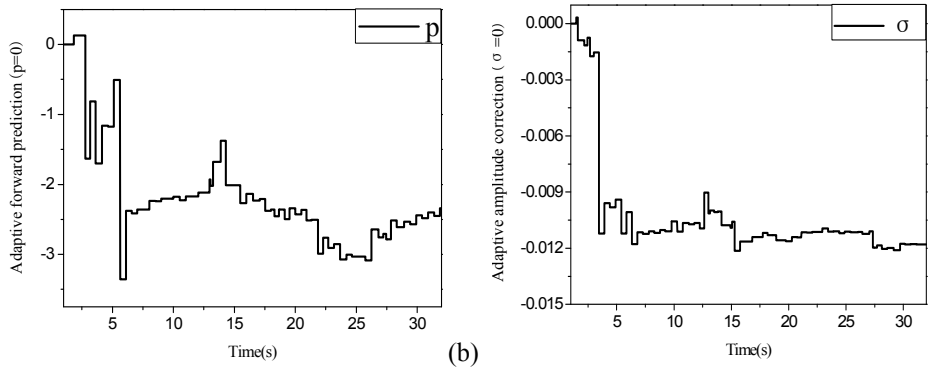

Figure 19. Adaptive parameter characteristics for Figure 16(a), (b). (a) Delay compensation adaption characteristics; (b) Amplitude error adaption characteristics.

From Fig. 18(a-b), it can be seen that the equivalent force response tracked the command well at the end of the time step. From Fig. 18(b), there are also some small errors in the peak EF, which are due to the large deadzone region of the actuator when it changes direction. From Fig. 18(c-d), it can be seen that the displacement response matched the exact solution well, although there are again small amplitude errors at the peak when the displacement is small because the noise in the displacement responses has relatively greater effect when the displacement response is small.

From Fig. 18(e), the equivalent force response of the EFC became unstable after some seconds because of the large time-delay. Note that the equivalent force response obtained by the EFC is multiplied by 4.5, which is the scale between the input signals of the two methods. It is clear that the equivalent force responses of the EFC are remarkably different from the responses of the EFC combined with an AFP. Because the input signals of the EFC are only 0.002g, its displacement response is nearly zero (approximately 0.01 mm). Thus, the noise and time delay make the test responses have great error at the beginning of the test. In summary, the EFC combined with an AFP gives significantly better accuracy than the EFC.

The adaptive parameter characteristics for earthquake input are shown in Fig. 19. It can be seen that the adaptive forward prediction and adaptive amplitude correction continue to adapt throughout the test period.

6.2 Magneto-rheological damper specimen real-time hybrid simulation

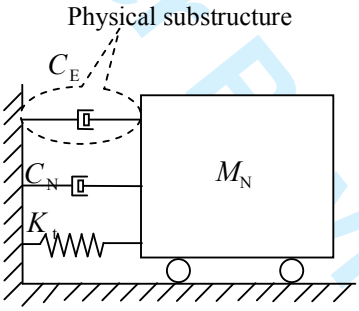

Figure 20. The substructured SDOF system.

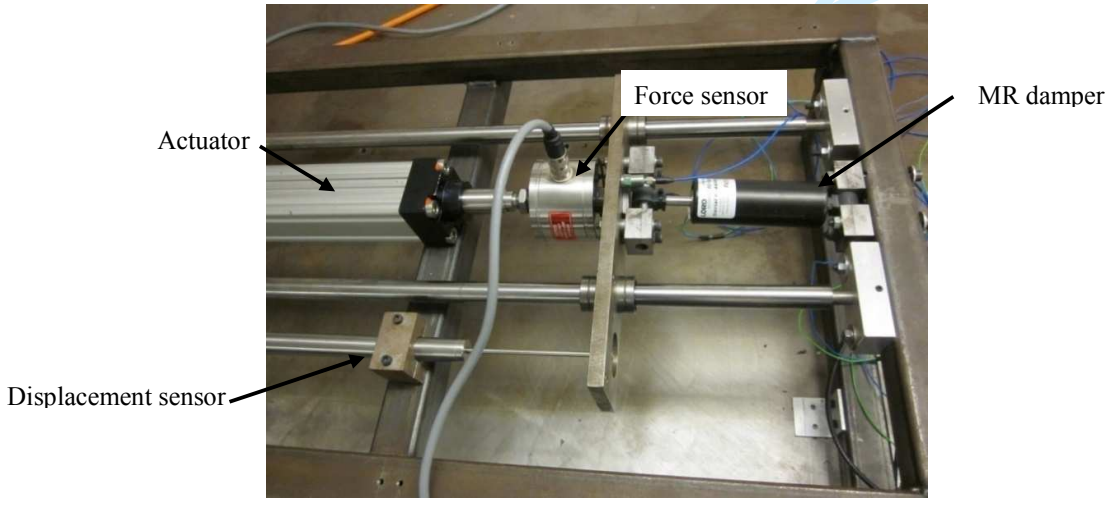

Figure 21. Experimental set-up of substructured model.

The structure to be emulated was an SDOF with M_N=720 kg, K_N=74400 Nm^{-1}, and ζ_N=0.02. The schematic diagram of the structure is shown in Fig. 20. The natural period of the structure was 1.6179 s. The physical part was a Magneto-rheological (MR) damper (RD-1005-3) produced by Lord Company; it was used as a passive damper with zero drive voltage. The excitation to the structure was El Centro (NS, 1940), with peak ground acceleration of 0.0625g. Fig. 21 shows the test set-up.

A proportional and feed forward controller was used to control the actuator, with controller gains of k_P=22 and k_{ff}=1.08. For the equivalent force control in this real-time hybrid simulation, the EFC controller with gains K_P=1, K_I=35 was adopted. The integration interval Δt was 0.01 s for the hybrid simulation. To smooth the actuator response, the equivalent force commands were interpolated linearly with time, and the sub-step interval was 0.001 s [7].

Three cases were considered in the tests: without compensation, the AFP compensation, and fixed compensation. The delay and amplitude error for the cases with fixed delay compensation were determined using the results without compensation: the data at the peak equivalent force command were used to determine the amplitude error, and the data at the zero equivalent force command closest to the peak were used to obtain the time delay. Correspondingly, P=3 and k_a=0.963 were obtained for fixed delay compensation. For the AFP, the parameters were P_0=3.5, k_{a0}=0.924, α=2.5×10^{-9}, β=1.25×10^{-10} and γ=2. Note that the initial values of P and k_a were obtained from the data of fixed delay compensation. The adaptive parameters, P and k_a, were constrained within the ranges [-1.5, 8.5] and [0.724, 1.124], respectively.

The equivalent force responses with an AFP algorithm, fixed compensation and without time delay compensation are shown in Fig. 22(a) and 22(b). The equivalent force errors are shown in Fig. 22(c) and Table 4. The force-displacement relationship for the MR damper during the test is shown in Fig. 23. Fig. 23 shows that the specimen has a clear nonlinear behavior. In Table 4, the maximum relative error, peak value error and normalized root-mean-square of error are defined as

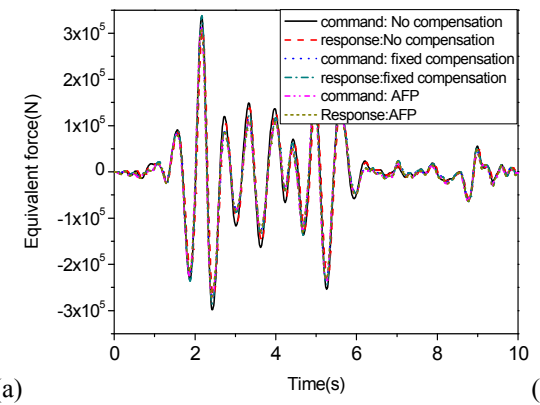

(a)

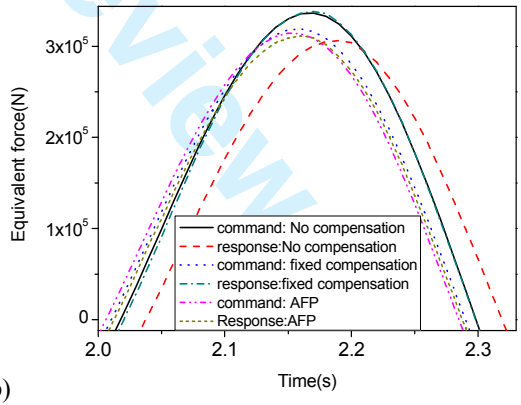

(b)

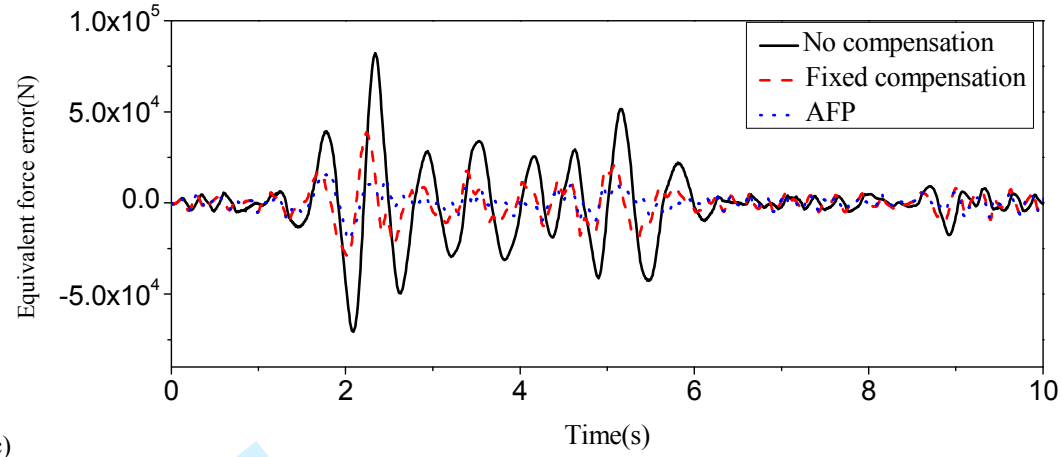

(c)

Figure 22. Comparison of responses with and without delay compensation. (a) Equivalent force response; (b) Enlarged view of equivalent force response; (c) Equivalent force error.

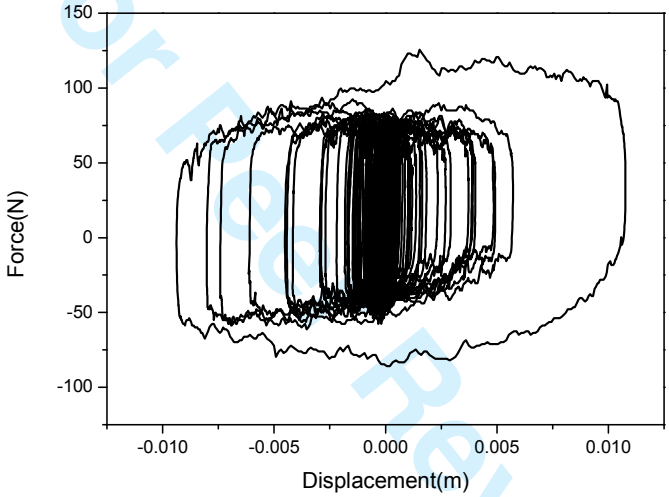

Figure 23. Force-displacement relationship of MR damper

Table 4 Equivalent force error comparison

Method	Without compensation	Fixed delay compensation	Adaptive delay compensation
Maximum error e_{EQ} (N)	8.22×10^4	3.89×10^4	1.93×10^4
Maximum relative error e_1 (%)	24.4	12.2	6.1
Peak value relative error e_2 (%)	9	5.9	0.92
The normalized RMS of error e_{RMS} (%)	22.59	11.44	6.47

$$e_1 = \left| \frac{\text{maximum of } e_{EQ}}{\text{maximum of } F_{EQ}^c} \right| \times 100\% \quad (45)$$

$$e_2 = \left| \frac{\text{maximum of } F_{\text{EQ}}^{\text{m}} - \text{maximum of } F_{\text{EQ}}^{\text{c}}}{\text{maximum of } F_{\text{EQ}}^{\text{c}}} \right| \times 100\% \tag{46}$$

$$e_{\text{RMS}} = \sqrt{\frac{\frac{1}{N}\sum_{i-1}^{N}(F_{\text{EQ}}^{\text{c}} - F_{\text{EQ}}^{\text{m}})^2}{\frac{1}{N}\sum_{i-1}^{N}(F_{\text{EQ}}^{\text{c}})^2}} \times 100\% \tag{47}$$

where N is the number of data points during RTHS.

From Fig. 22(a-c), it can be seen that the equivalent force response tracked the command the best with an AFP. The delay and amplitude errors are clearly seen in Fig. 22(b) for the case without time delay compensation. The responses were improved with the fixed compensation, but a small overshoot could still be seen. With an AFP, the response matched the command almost perfectly. The advantage of the AFP is further revealed quantitatively from the data in Table 4.

7. CONCLUSION

The AFP algorithm is used to improve the performance of the EFC for real-time hybrid simulation. The stability of this new method is studied by analyzing the pole locations in the discrete transfer function. The limiting values for the adaptive parameters P and k_a are set based on this analysis. The results show that the stability limit of the new method for both stiffening and softening structures is larger than that of the EFC. Numerical simulation results of RTHS with linear and stiffening specimens are presented. Simulation results show that the AFP version has better stability and accuracy than the unmodified EFC. RTHS with a linear stiffness spring specimen is conducted using seismic waves as the input. Test results indicate that the AFP algorithm can adaptively compensate for the time delay of the equivalent force control system. Finally, the experimental results with an MR damper specimen demonstrate that the EFC-AFP algorithm has better accuracy than the unmodified EFC and EFC with fixed compensation when applied to a nonlinear experimental structure.

ACKNOWLEDGEMENT

First, the authors are grateful to Prof. Wu and Dr. Xu of Harbin Institute of Technology; the amendments of an editorial nature and topic structure revision were finished under their guidance. The authors are grateful to Mr. Rendall and Mr. Griffith of the Bristol Laboratory for Advanced Dynamics Engineering, University of Bristol, for their assistance with the operation of the dSPACE testing system and Jack Potter's suggestions for the tests. The research is financially supported by the National Key Research and Development Program of China (Grant No. 2016YFC0701106), the Scientific Research Fund of the Institute of Engineering Mechanics, China Earthquake Administration (2016B09) and National Science Foundation of China (51408565, 51378478, 51161120360, 91315301-09).

REFERENCE

1. Nakashima M, Kato H, Takaoka E. Development of real-time pseudodynamic testing. *Earthquake Engineering and Structural Dynamics* 1992; **21**:779-792.
2. Carrion JE, Spencer BF. Model-based strategies for real-time hybrid testing. *NSEL Report Series Report No. NSEL-006*, December 2007.
3. Jung RY, Shing PB, Stauffer E, Thoen B. Performance of a real-time pseudo dynamic test system

considering nonlinear structural response. *Earthquake Engineering and Structural Dynamics* 2007; **36**(12):1785-1809.

4. Kolay C, James MR, Thomas MM, Mahvashmohammadi A, Richard S. Implementation and application of the unconditionally stable explicit parametrically dissipative KR-α method for real-time hybrid simulation. *Earthquake Engineering and Structural Dynamics* 2015; **44**(5):735-755.
5. Bursi OS, Jia C, Vulcan L, Neild SA, Wagg DJ. Rosenbrock-based algorithms and subcycling strategies for real-time nonlinear substructure testing. *Earthquake Engineering and Structural Dynamics* 2011; **40**:1-19.
6. Chen C, Ricles JM. Stability analysis of explicit integration algorithms with actuator delay in real-time hybrid testing. *Earthquake Engineering and Structural Dynamics* 2008; **37**: 597-613.
7. Wu B, Wang Q, Shing PB, Ou J. Equivalent force control method for generalized real-time substructure testing with implicit integration. *Earthquake Engineering and Structural Dynamics* 2007; **36**(9):1127-1149.
8. Wu B, Xu G, Li Y, Shing P, Ou J. Performance and application of equivalent force control method for real-time substructure testing. *Journal of Engineering Mechanics (ASCE)* 2012; **138**(11):1303-1316.
9. Wu B, Xu G, Shing PB. Equivalent force control method for real-time testing of nonlinear structures. *Journal of Earthquake Engineering* 2011; **15**:143-164.
10. Wu B, Zhou H.Sliding mode for equivalent force control in real-time substructure testing. *Structural Control and Health Monitoring* 2014; **21**(10):1284-1303.
11. Horiuchi T, Inoue M, Konno T, Namita Y. Real-time hybrid experimental system with actuator delay compensation and its application to a piping system with energy absorber. *Earthquake Engineering and Structural Dynamics* 1999; **28**:1121-1141.
12. Shi P, Wu B, Spencer BF, Philips BM, Chang C. Real-time hybrid testing with equivalent force control method incorporating Kalman filter. *Structural Control and Health Monitoring* (online); DOI:10.1002/stc.1808.
13. Christenson R, Lin YZ, Emmons A, Bass B. Large-scale experimental verification of semiactive control through real-time hybrid simulation. *Journal of Structure Engineering (ASCE)* 2008; **134**(4):522-534.
14. Wallace MI, Wagg DJ, Neild SA. An adaptive polynomial based forward prediction algorithm for multi-actuator real-time dynamic substructuring. *Proc. R Soc. A* 2005; **461**(2064): 3807-3826.
15. Horiuchi T, Konno T. A new method for compensating actuator delay in real-time hybrid experiments. *Phil. Trans. R. Soc. Lond. A* 2001; **359**:1893-1909.
16. Darby AP, Williams MS, Blakeborough A. Stability and delay compensation for real-time substructure testing. *Journal of Engineering Mechanics (ASCE)* 2002; **128**(12): 1276-1284.
17. Ahmadizadeh M, Mosqueda G, Reinhorn AM. Compensation of actuator delay and dynamics for real-time hybrid structural simulation. *Earthquake Engineering and Structural Dynamics* 2008; **37** (1):21-42.
18. Chen PC, Tsai KC. Dual compensation strategy for real-time hybrid testing. *Earthquake Engineering and Structural Dynamic* 2013; **42**:1-23.
19. Wu B, Wang Z, and Bursi OS. Actuator dynamics compensation based on upper bound delay for real-time hybrid simulation. *Earthquake Engineering and Structural Dynamics* 2013; **42**(12): 1749-1765.
20. Wang Z, Wu B, Bursi OS, Xu G, Ding Y. An effective online delay estimation method based on a simplified physical system model for real-time hybrid simulation. *Smart Structures and systems* 2014; **14**(6):1247-1267.

21. Chae Y, Kazemibidokhti K, Ricles JM. Adaptive time series compensator for delay compensation of servo-hydraulic actuator systems for real-time hybrid simulation. *Earthquake Engineering and Structural Dynamics* 2013; **42**(11): 1697-1715.
22. Wallace MI, Sieber J, Neild SA, Wagg DJ, Krauskopf B. Stability analysis of real-time dynamic substructuring using delay differential equation models. *Earthquake Engineering and Structural Dynamics* 2005; **34**(11): 1817-1832.
23. Tu J, Hsiao W, Chen C. Modelling and control issues of dynamically substructured systems: adaptive forward prediction taken as a example. *Proc. R Soc. A* 2014; **470**(2168): 1-17.
24. Zhao J, French C, Shield C, Posbergh T. Considerations for the development of real-time dynamic testing using servo-hydraulic actuation. *Earthquake Engineering and Structural Dynamics* 2003; **32**:1773-1794.
25. Phillips BM, Spencer JF. Model-based feedforward-feedback actuator control for real-time hybrid simulation. *Journal of Structure Engineering (ASCE)* 2012; **139**, SPECIAL ISSUE: NEES1: Advances in Earthquake Engineering, 1205-1214.
26. Chen P, Chang C, Spencer BF, Tsai K. Adaptive model-based tracking control for real-time hybrid simulation. *Bull Earthquake Eng* 2015; **13**:1633-1653.
27. Ou G, Ozdagli AI, Dyke SJ, and Wu B. Robust integrated actuator control: experimental verification and real-time hybrid-simulation implementation. *Earthquake Engineering and Structural Dynamics* 2014; DOI: 10.1002/eqe.2479.
28. Liu J, Dyke SJ, Liu H, Gao X, Philips B. A novel integrated compensation method for actuator dynamics in real-time hybrid structural testing. *Structural Control and Health Monitoring* 2013; **20**(7):1057-1080.
29. Chen C, Ricles JM. Improving the inverse compensation method for real-time hybrid simulation through a dual compensation scheme. *Earthquake Engineering and Structural Dynamics* 2009; **38**:1237-1255.
30. Chen C, Ricles JM, Sause R, Christenson R. Experimental evaluation of an adaptive inverse compensation technique for real-time simulation of a large-scale magneto-rheological fluid damper. *Smart Materials and Structures* 2010; **19**:1-12.
31. Chen C, Ricles JM, Guo T. Improved adaptive inverse compensation technique for real-time hybrid simulation. *Journal of Engineering Mechanics* 2012; **138**(12):1432-1446.
32. Burden R, Faires J. *Numerical Analysis* (7th edn). Thomson Learning. (Reprinted by Higher Education Press, Beijing, 2001).
33. Wallace MI. Real-time dynamic substructuring for mechanical and aerospace applications; control techniques and experimental methods. *Bristol: University of Bristol Thesis* 2006:115-120.
34. ÅstrÖm KJ, Wittenmark B.*Adaptive control*. Addison Wesley 1995.
35. Chen C, Ricles JM. Stability analysis of direct integration algorithms applied to nonlinear structural dynamics. *Journal of Engineering Mechanics* 2008; **134**(9):703-711.
36. Chen C, Ricles JM. Analysis of implicit HHT-α integration algorithm for real-time hybrid simulation. *Earthquake Engineering and Structure Dynamic* 2011; **41**(5):1021-1041.
37. Chen C, Ricles JM. Analysis of actuator delay compensation methods for real-time testing. *Engineering Structures* 2009; **31**(11):2643-2655.
38. Zhu F, Wang J, Jin F, Chi F and Gui Y. Stability analysis of MDOF real-time dynamic hybrid testing systems using the discrete-time root locus technique. *Earthquake Engineering and Structure Dynamic* 2015; **44**(2):221-241.

39. ÅstrÖm KJ, Wittenmark B. *Computer-controlled systems theory and design* (3th edn). Prentice Hall (Reprinted by Tsinghua University Press & Prentice Hall, Beijing, 2002).